

Title	Robustness of enhanced shortcuts to adiabaticity in lattice transport
Authors	Whitty, Chris;Kiely, A.;Ruschhaupt, Andreas
Publication date	2022-01-13
Original Citation	Whitty, C., Kiely, A. and Ruschhaupt, A. (2022) 'Robustness of enhanced shortcuts to adiabaticity in lattice transport', Physical Review A, 105(1), 013311 (13pp). doi: 10.1103/PhysRevA.105.013311
Type of publication	Article (peer-reviewed)
Link to publisher's version	10.1103/PhysRevA.105.013311
Rights	© 2022, American Physical Society.
Download date	2025-06-20 06:15:58
Item downloaded from	https://hdl.handle.net/10468/12564



UCC

University College Cork, Ireland
Coláiste na hOllscoile Corcaigh

Robustness of enhanced shortcuts to adiabaticity in lattice transportC. Whitty^{1,*}, A. Kiely^{2,3} and A. Ruschhaupt¹¹*Department of Physics, University College Cork, Cork, Ireland*²*School of Physics, University College Dublin, Belfield, Dublin 4, Ireland*³*Centre for Quantum Engineering, Science, and Technology, University College Dublin, Belfield, Dublin 4, Ireland*

(Received 14 September 2021; accepted 14 December 2021; published 13 January 2022)

Shortcuts to adiabaticity (STA) are a collection of quantum control techniques that achieve high fidelity outside of the adiabatic regime. Recently an extension to shortcuts to adiabaticity was proposed by the authors [Whitty, Kiely, and Ruschhaupt, *Phys. Rev. Research* **2**, 023360 (2020)]. This method, enhanced shortcuts to adiabaticity (eSTA), provides an extension to the original STA control functions and allows effective control of systems not amenable to STA methods. It is conjectured that eSTA schemes also enjoy an improved stability over their STA counterparts. We provide numerical evidence of this claim by applying eSTA to fast atomic transport using an optical lattice and evaluating appropriate stability measures. We show that the eSTA schemes not only produce higher fidelities but also remain more stable against errors than the original STA schemes.

DOI: [10.1103/PhysRevA.105.013311](https://doi.org/10.1103/PhysRevA.105.013311)**I. INTRODUCTION**

Quantum devices and technologies have the potential to revolutionize a broad range of scientific and engineering disciplines [1,2]. However, fast and stable control of these systems is a significant barrier to building practical devices [3]. Quantum control needs to be fast to avoid decoherence, while simultaneously being robust and stable against implementation errors. Furthermore, it should be effective within the constrained resources of the physical implementation, such as energetic cost or pulse bandwidth [4].

Often practical quantum control relies heavily on numerical optimization, which has some drawbacks: it can be computationally expensive and difficult to scale, and it may be unclear how to understand or generalize the resulting schemes [5–7]. Analytical control techniques have been developed for specific control problems, for example, transport of a rigid harmonic trap [8]. There exist further analytic techniques, such as shortcuts to adiabaticity (STA), which can also give exact quantum state transfer. However, analytic techniques such as STA are known exactly for only a limited number of physical systems [9–11]. Recently an extension to STA methods has been developed, known as enhanced shortcuts to adiabaticity (eSTA), that provides control for a broader class of systems [12]. Crucially, eSTA is an analytic technique that allows physical insight into the control scheme. Additionally, eSTA has a much lower computation cost compared with full numerical optimization. eSTA has been applied to population inversion in a two-level system without the rotating-wave approximation and to the transport of a Gaussian trap with one and two ions [12]. Recently, there has already been an application of eSTA techniques to the transport of atoms in an optical lattice [13].

STA schemes are extremely robust to noise and systematic errors [14–18]. An obvious question is whether robustness remains in the eSTA framework. Therefore, the main goal of this paper is to provide a thorough investigation into how this stability is affected by the application of eSTA.

We choose atomic transport using an optical lattice to examine the robustness of eSTA, since the coherent control of lattice systems has many practical quantum technological applications, for example, transport in atomic chains [19], modeling condensed matter systems [20], many-body phenomena in ultracold gases [21], and the trapping and control of ions [22,23]. Optical lattices with optical tweezers have also been used as an architecture for quantum computation [24,25], with optimal control derived transport [26] and optimized spatial adiabatic passage [27]. Recently, there has been experimental and theoretical exploration of atom transport via a lattice potential around the quantum speed limit [28]. We consider similar physical parameters with transport times near this proposed speed limit [28,29]. We then show that the eSTA schemes provide improved robustness over the corresponding STA schemes, when considering a variety of imperfections.

In the following section we give a brief review of the formalism of eSTA. In Sec. III we present the physical optical lattice model we are considering; we introduce different control schemes and we examine and compare the fidelities achieved by eSTA. In Sec. IV, we first define and then examine the deviation of the eSTA control function under variations of the Hamiltonian. This gives a preliminary indication of the stability of eSTA. In the following sections we compare the stability of eSTA and STA in more detail. This includes a definition of a sensitivity quantity and an error bound for a quantitative comparison of the stability of different schemes. In Sec. V we consider systematic errors during the transport. In Sec. VI the stability of lattice transport is examined for noisy fluctuations.

*c.whitty@umail.ucc.ie

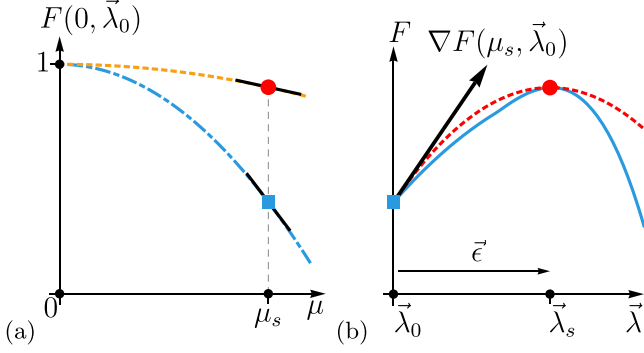


FIG. 1. (a) Schematic representation of fidelity versus μ . The fidelity of \mathcal{H}_μ using $\vec{\lambda}_0$ is the dash-dotted blue line. The blue square is \mathcal{H}_{μ_s} using $\vec{\lambda}_0$. The red dot is the improved fidelity of \mathcal{H}_{μ_s} using $\vec{\lambda}_s$. The dashed orange line represents the assumed parabolic profile of the fidelity as $\mathcal{H}_0 \rightarrow \mathcal{H}_{\mu_s}$, with the improved eSTA control $\vec{\lambda}_{\mu_s}$ calculated for each μ . The slopes of each line at μ_s are depicted as solid black lines. (b) Diagram of eSTA in control space $(\vec{\lambda}, F)$. The fidelity of the starting STA control vector $\vec{\lambda}_0$ (blue square) and the resulting fidelity using the eSTA control vector $\vec{\lambda}_s = \vec{\lambda}_0 + \vec{\epsilon}$ (red dot) are shown. Also highlighted are the gradient (black arrow), the approximate eSTA parabola (dashed red line), and the true fidelity landscape (solid blue line).

II. eSTA FORMALISM

The purpose of eSTA is to provide a formalism by which existing STA methods can be extended to quantum control problems beyond their current scope.

We start with a system with the Hamiltonian \mathcal{H}_s that has a difficult quantum control problem. However, we assume that the Hamiltonian \mathcal{H}_s can be approximated by another Hamiltonian \mathcal{H}_0 of an idealized system that has an exact STA solution. In the following we construct the improved eSTA protocol for \mathcal{H}_s using the solutions of the idealized system \mathcal{H}_0 .

A. Construction of eSTA control scheme

To make the approximation of \mathcal{H}_s by \mathcal{H}_0 precise, we assume there is a parameter μ and Hamiltonians \mathcal{H}_μ such that $\mathcal{H}_{\mu=\mu_s} = \mathcal{H}_s$ and $\mathcal{H}_{\mu=0} = \mathcal{H}_0$. We also assume we can parametrize the control scheme by a vector $\vec{\lambda}$. We set $\vec{\lambda}_0$ to denote the STA scheme and set $\vec{\lambda}_s$ to denote the eSTA scheme.

Our goal is to evolve the initial state $|\Psi_0\rangle$ at time $t = 0$ to the target state $|\Psi_T\rangle$ in a given total time t_f . As previously discussed, we assume there exists an idealized system with known STA solutions and Hamiltonian $\mathcal{H}_0(\vec{\lambda}_0; t)$. $\vec{\lambda}_0$ solves the control problem for \mathcal{H}_0 , and we assume it works approximately for \mathcal{H}_{μ_s} .

To state this formally we define the fidelity

$$F(\mu, \vec{\lambda}) = |\langle \Psi_T | U_{\mu, \vec{\lambda}}(t_f, 0) | \Psi_0 \rangle|^2, \quad (1)$$

where $U_{\mu, \vec{\lambda}}$ is the time-evolution operator using the Hamiltonian \mathcal{H}_μ with the control scheme $\vec{\lambda}$. We have that $F(\mu_s, \vec{\lambda}_0) < F(0, \vec{\lambda}_0) = 1$ [see also Fig. 1(a)].

The goal of eSTA is to produce a $\vec{\lambda}_s$ that is built upon $\vec{\lambda}_0$, such that we maximize $F(\mu_s, \vec{\lambda}_s)$ with $F(\mu_s, \vec{\lambda}_s) > F(\mu_s, \vec{\lambda}_0)$. We define $\vec{\lambda}_s = \vec{\lambda}_0 + \vec{\epsilon}$, and eSTA is now used to calculate $\vec{\epsilon}$.

We assume in the following that μ_s is small and that the fidelity landscape about H_0 at $\mu = 0$ and $\vec{\lambda} = \vec{0}$ is smooth and can be approximated well if considering only up to second order in μ and $\vec{\lambda}$.

To find $\vec{\epsilon}$, we use information about the fidelity and the gradient of the fidelity with respect to $\vec{\lambda}$ to construct a parabola in the parameter space of $\vec{\lambda}$ and F , as illustrated in Fig. 1(b). We assume that this parabola is a good approximation to the fidelity landscape in the direction of the gradient at $(\mu_s, \vec{\lambda}_0)$. The form of the parabola follows from, and is consistent with, the approximation of the fidelity landscape only up to second order in μ and $\vec{\lambda}$. This is schematically shown in Fig. 1(b), with the dashed red line representing the parabolic approximation and the solid blue line denoting the actual fidelity landscape. Furthermore we assume that the maximum of this parabola gives perfect fidelity, i.e., $F(\mu_s, \vec{\lambda}_0 + \vec{\epsilon}) \approx 1$. We can then write

$$\vec{\epsilon} \approx \frac{2[1 - F(\mu_s, \vec{\lambda}_0)] \nabla_{\vec{\lambda}} F(\mu_s, \vec{\lambda}_0)}{|\nabla_{\vec{\lambda}} F(\mu_s, \vec{\lambda}_0)| |\nabla_{\vec{\lambda}} F(\mu_s, \vec{\lambda}_0)|}. \quad (2)$$

We now calculate $\vec{\epsilon}$ using an approximation of the gradient and fidelity at the point $(\mu_s, \vec{\lambda}_0)$, shown as the blue square in Fig. 1. We begin the derivation of these estimates by assuming that the initial state $|\Psi_0\rangle$ and the final target state $|\Psi_T\rangle$ are both the same for the \mathcal{H}_0 and \mathcal{H}_{μ_s} systems. We assume that the idealized \mathcal{H}_0 system can be treated with STA techniques, i.e., there is a solution $|\chi_0(t)\rangle$ of the time evolution leading to a fidelity of 1, with $|\chi_0(0)\rangle = |\Psi_0\rangle$ and $|\chi_0(t_f)\rangle = |\Psi_T\rangle$. In addition, we assume that there are solutions of the time evolution of \mathcal{H}_0 labeled $\{|\chi_n(t)\rangle\}_{n \in \mathbb{N}}$ such that $\{|\chi_n(t)\rangle\}_{n \in \mathbb{N}_0}$ form an orthonormal basis for solutions of the \mathcal{H}_{μ_s} system. So we have

$$|\chi_n(t)\rangle = U_{0, \vec{\lambda}_0}(t, 0) |\chi_n(0)\rangle, \quad (3)$$

$$U_{0, \vec{\lambda}_0}(t, s) = \sum_n |\chi_n(t)\rangle \langle \chi_n(s)|. \quad (4)$$

Note that in the following examples, we use invariant-based inverse engineering to design the STA solutions and in these cases $\{|\chi_n(t)\rangle\}_{n \in \mathbb{N}_0}$ are (up to a phase) the instantaneous eigenstates of the corresponding invariant.

We use time-dependent perturbation theory to calculate an approximation of the fidelity $F(\mu_s, \vec{\lambda}_0)$ and the gradient of the fidelity $\nabla F(\mu_s, \vec{\lambda}_0)$. We assume that we can neglect higher-order contributions in both μ and $\vec{\epsilon}$. The details of the calculations can be found in Ref. [12]. For the fidelity $F(\mu_s, \vec{\lambda}_0)$ we then obtain up to second order in μ_s

$$F(\mu_s, \vec{\lambda}_0) \approx 1 - \frac{1}{\hbar^2} \sum_{n=1}^{\infty} |G_n|^2, \quad (5)$$

where

$$G_n = \int_0^{t_f} dt \langle \chi_n(t) | [\mathcal{H}_{\mu_s}(\vec{\lambda}_0; t) - H_0(\vec{\lambda}_0; t)] | \chi_0(t) \rangle. \quad (6)$$

For the gradient approximation we find

$$\nabla F(\mu_s, \lambda_0) \approx -\frac{2}{\hbar^2} \sum_{n=1}^{\infty} \text{Re}(G_n \vec{K}_n^*), \quad (7)$$

with

$$\vec{K}_n = \int_0^{t_f} dt \langle \chi_n(t) | \nabla \mathcal{H}_{\mu_s}(\vec{\lambda}_0; t) | \chi_0(t) \rangle. \quad (8)$$

Using Eq. (2), we can now write the analytical expression for the eSTA protocol $\vec{\lambda}_s \approx \vec{\lambda}_0 + \vec{\epsilon}$ as

$$\vec{\epsilon} = - \frac{(\sum_{n=1}^N |G_n|^2) [\sum_{n=1}^N \text{Re}(G_n^* \vec{K}_n)]}{|\sum_{n=1}^N \text{Re}(G_n^* \vec{K}_n)|^2}, \quad (9)$$

where G_n is given by Eq. (6), K_n is given by Eq. (8), and we have truncated the infinite sums to the first N terms.

It is important to note that G_n and \vec{K}_n can both be easily calculated as only the Hamiltonians and the known STA solutions for the idealized system with Hamiltonian \mathcal{H}_0 are needed. We also note that eSTA can produce protocols which are outside the class of STA schemes and offers improvement over previous perturbation-based optimization [12].

B. Expected stabilities of eSTA and STA

We now provide a general heuristic argument of why it is expected that eSTA protocols not only have improved fidelity but also have improved stability compared with their corresponding STA schemes. Let us consider Fig. 1(a), showing schematically the fidelity versus μ ; $\mu = 0$ corresponds with the approximated system and μ_s the system of interest. The fidelity of \mathcal{H}_μ using the initial STA control scheme $\vec{\lambda}_0$ is the dot-dashed blue line; the dashed orange line represents the fidelity using the improved eSTA control $\vec{\lambda}_\mu$ calculated for each μ . Since the STA and eSTA control schemes agree at $\mu = 0$, the fidelity must be 1 for both at this point. By construction, for a given μ the fidelity produced using the eSTA control scheme (dashed orange line) is higher than the corresponding one for the STA scheme (dot-dashed blue line). Assuming that the fidelity behaves as a parabola, the magnitude of the slope of the eSTA fidelity must be less than the slope of the STA fidelity at μ_s .

We now consider the effect of a systematic error δ , such that the STA and eSTA schemes derived using μ_s are now applied to the system at a different, nearby $\mu = \mu_s(1 + \delta)$. We expect that the derivative of the fidelity in both cases can be approximated by the slopes shown in Fig. 1(a) (solid black lines). Therefore, the fidelity in the eSTA case should vary less than the fidelity in the STA case. Thus, the eSTA protocol should have higher stability against changes in μ than the corresponding STA scheme. To confirm this intuitive reasoning, in the following we examine the stability in more detail.

III. PHYSICAL MODEL

We consider atomic transport in an optical lattice that currently has no STA solution. For sufficient trapping depths the lattice potential can be well approximated locally by a harmonic potential. The transport of a harmonic potential has an exact STA solution for all transport times using Lewis-Riesenfeld invariants [10,11]. Hence, we choose the harmonic potential transport STA solutions as the starting point to produce an eSTA protocol for the lattice transport problem.

The lattice potential is given by

$$V_S(x) = U_0 \sin^2(k_0 x), \quad (10)$$

where $U_0 = \alpha E_{\text{rec}}$, $E_{\text{rec}} = 2(\pi \hbar)^2 / m \lambda^2$, and $k_0 = 2\pi / \lambda$. The motion of the lattice is described by a function $q_0(t)$, and Hamiltonian $\mathcal{H}_{\mu_s} = H_S$, where

$$H_S = \frac{p^2}{2m} + V_S[x - q_0(\vec{\lambda}, t)]. \quad (11)$$

For designing the STA trajectories, we apply a harmonic approximation to the potential V_S . A series expansion of $V_S(x)$ results in

$$V_S(x) = V_0(x) + O(x^4), \quad (12)$$

where

$$V_0(x) = \frac{1}{2} m \omega_0^2 x^2, \quad (13)$$

and $\omega_0 = \sqrt{\frac{2U_0}{m}} k_0 = \sqrt{\alpha} (4\pi^2 \hbar) / m \lambda^2$. The corresponding idealized Hamiltonian $\mathcal{H}_0 = H_0$ is

$$H_0 = \frac{p^2}{2m} + V_0[x - q_0(\vec{\lambda}, t)]. \quad (14)$$

Note that in this case as $U_0 \rightarrow \infty$, $H_S \rightarrow H_0$.

We also define a time unit $\tau = 2\pi / \omega_0$ and a spatial unit $\sigma = \sqrt{\hbar / (m\omega_0)}$.

A. STA control functions

There exist known STA techniques to design trajectories $q_0(t)$ that give fidelity $F = 1$ for the harmonic potential H_0 and arbitrary transport times [10,11]. In the following, we will use Lewis-Riesenfeld invariants to obtain STA trajectories for H_0 [11,30]. For harmonic trap a known dynamical invariant has the form [11]

$$I(t) = \frac{1}{2m} (p - m\dot{q}_c)^2 + \frac{1}{2} m \omega_0^2 [x - m q_c(t)]^2, \quad (15)$$

where $q_c(t)$ must satisfy the auxiliary equation

$$\ddot{q}_c + \omega_0^2 (q_c - q_0) = 0. \quad (16)$$

Note that Eq. (16) describes a single-particle classical equation of motion, where $q_0(t)$ is the trajectory of the potential minimum and $q_c(t)$ is the resulting classical particle trajectory.

Solutions of the Schödinger equation $i\hbar \partial / \partial t \Psi(x, t) = H_0 \Psi(x, t)$ can be expressed in terms of weighted transport modes,

$$\Psi(x, t) = \sum_n c_n e^{i\theta_n(t)} \psi_n(x, t), \quad (17)$$

where $\psi_n(x, t)$ are orthonormal eigenstates of the invariant I satisfying $I(t) \psi_n(x, t) = \lambda_n \psi_n(x, t)$, c_n are constants, and the Lewis-Riesenfeld phase is given by

$$\theta_n(t) = \frac{1}{\hbar} \int_0^t \langle \phi(t', n) | i\hbar \frac{\partial}{\partial t'} - H_0(t') | \phi(t', n) \rangle dt'. \quad (18)$$

In the specific case of harmonic transport, the resulting transport modes in Eq. (17) are

$$\chi_n(x, t) = e^{i\theta_n(t)} \psi_n(x, t) = e^{i\theta_n(t)} e^{\frac{i}{\hbar} m \dot{q}_c x} \phi_n(x - q_c), \quad (19)$$

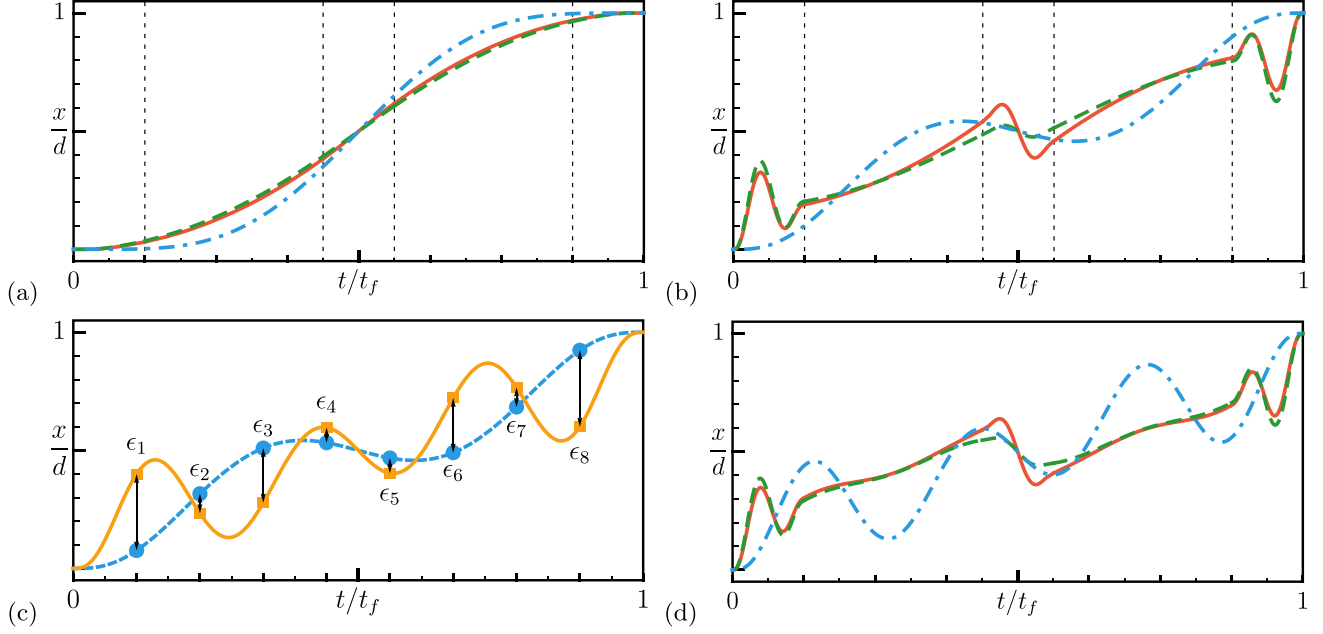


FIG. 2. Plot of STA and eSTA control functions. All of these plots use $t_f/\tau = 0.8$ and $d = \lambda/2$ (one lattice site). The vertical dashed lines in panels (a) and (b) indicate the smoothing boxes of length $t_f/8$ about the discontinuities in $q_{c,2}$ and $q_{c,3}$. (a) Plot of the auxiliary functions $q_{c,1}(t)$ (dot-dashed blue), $q_{c,2}(t)$ (dashed green), and $q_{c,3}(t)$ (solid red). (b) Corresponding plots of the STA transport functions $q_{0,1}(t)$ (dot-dashed blue), $q_{0,2}(t)$ (dashed green), and $q_{0,3}(t)$ (solid red). (c) Example of the vector components of the eSTA correction $\bar{\epsilon}$, with $q_{0,1}$ (dashed blue) and Q_1 (solid orange). (d) Examples of the eSTA control functions $Q_1(t)$ (dot-dashed blue), $Q_2(t)$ (dashed green), and $Q_3(t)$ (solid red).

where

$$\theta_n(t) = -\frac{i}{\hbar}[(n+1/2)\hbar\omega_0]t + \int_0^t \frac{m\dot{q}_c^2}{2} dt', \quad (20)$$

with $\lambda_n = (n+1/2)\hbar\omega_0$, and $\phi_n(x)$ are solutions to the Schrödinger equation at $t=0$, i.e., harmonic eigenstates.

To ensure $I(t)$ and $H_0(t)$ agree at initial and final times, we set $[I(t), H_0(t)] = 0$ for $t=0$ and t_f . This is equivalent [via Eqs. (16) and (19)] to the boundary conditions

$$\begin{aligned} q_c(0) &= 0, & q_c(t_f) &= d, \\ \dot{q}_c(0) &= \ddot{q}_c(0) = 0, & \dot{q}_c(t_f) &= \ddot{q}_c(t_f) = 0. \end{aligned} \quad (21)$$

The key idea is that $q_c(t)$ can be chosen first, for example, to be a polynomial that satisfies the boundary conditions in Eq. (21), and then $q_0(t)$ can be inverse engineered using Eq. (16).

Throughout this paper we enforce further boundary conditions on $q_c(t)$, namely,

$$q_c^{(3)}(t') = q_c^{(4)}(t') = 0, \text{ for } t = 0, t_f, \quad (22)$$

so that the resulting trap trajectory $q_0(t)$ ensures the trap is at rest for initial and final times. In the following, we use three different auxiliary functions $q_c(t)$ and calculate the corresponding STA trajectories $q_0(t)$.

Polynomial function $q_{c,1}(t)$. One of the simplest choices for an auxiliary function is a polynomial ansatz $q_{c,1}(t)$ [11], i.e.,

$$q_{c,1}(t) = \sum_{j=1}^J a_j t^j, \quad (23)$$

where J is the number of boundary conditions. For the boundary conditions in Eqs. (21) and (22), $J = 10$ and we solve for

the a_j to get $q_{c,1}(t)$. We then use Eq. (16) to produce $q_{0,1}(t)$. Examples of $q_{c,1}(t)$ and $q_{0,1}(t)$ can be seen in Figs. 2(a) and 2(b), respectively (blue dot-dashed lines).

Quasioptimal function $q_{c,2}(t)$. Moving beyond the simple polynomial ansatz for q_c , we consider a trajectory introduced in Ref. [31] as a quasioptimal solution to minimizing the quartic term in the potential $(1/2)m\omega_0^2[x - q_0(t)]^2 - \beta[x - q_0(t)]^4$. We label this auxiliary function $q_{c,2}(t)$ and our motivation for using this function is that it should reduce the effect of the anharmonic contribution within H_S . This auxiliary function was derived using Pontryagin's maximal principle and relies on first calculating a function f_c that minimizes the quartic term contribution to the potential during transport [31],

$$f_c(t) = \frac{3d}{8} \left(1 - 2\frac{t}{t_f}\right)^{7/3} + \frac{7d}{4} \frac{t}{t_f} - \frac{3d}{8}. \quad (24)$$

This function f_c does not satisfy the boundary conditions in Eq. (21) and it is the root of a complex-valued equation [31]. We simplify the definition of f_c , by mapping f_c from $(0, t_f/2)$ to $(t_f/2, t_f)$ appropriately. We also enforce the boundary conditions from Eq. (21),

$$q_{c,2}(t) = \begin{cases} 0, & t \leq 0, \\ f_c(t), & 0 < t < t_f/2, \\ -f_c(t_f - t) + d, & t_f/2 < t < t_f, \\ d, & t \geq t_f. \end{cases} \quad (25)$$

To calculate $q_{0,2}(t)$, it is convenient to define $f_u(t) = 1/\omega_0^2 f_c''(t_f - t)$, where

$$f_u(t) = \frac{14d}{3\omega_0^2 t_f^2} \left(2\frac{t}{t_f} - 1\right)^{1/3}. \quad (26)$$

Similarly we first consider f_u on $(t_f/2, t_f)$ and map appropriately to $(0, t_f/2)$, and we obtain

$$q_{0,2}(t) = \begin{cases} 0, & t \leq 0, \\ f_c(t) + f_u(t_f - t), & 0 < t < t_f/2, \\ -f_c(t_f - t) - f_u(t) + d, & t_f/2 < t < t_f, \\ d, & t \geq t_f, \end{cases} \quad (27)$$

which has discontinuities at $t = 0$, $t = t_f/2$, and $t = t_f$. These jump points may be difficult to implement practically, so we smooth $q_{c,2}(t)$ in a time interval of length t_T around the jump points, using polynomial interpolation. Later we show that high performance can be achieved even with this smoothing process and that the exact time-interval chosen is not critical to robust and high-fidelity transport. Using Eq. (16) we can now calculate $q_{0,2}(t)$ as

$$q_{0,2}(t) = \begin{cases} p_0''(t)/\omega_0^2 + p_0(t), & 0 \leq t < t_0, \\ f_c(t) + f_u(t_f - t), & t_0 \leq t \leq t_1, \\ p_1''(t)/\omega_0^2 + p_1(t), & t_1 < t < t_2, \\ -f_c(t_f - t) - f_u(t) + d, & t_2 \leq t \leq t_3, \\ p_2''(t)/\omega_0^2 + p_2(t), & t_3 < t \leq t_f, \end{cases} \quad (28)$$

where $t_0 = t_T$, $t_1 = (t_f - t_T)/2$, $t_2 = (t_f + t_T)/2$, and $t_3 = t_f - t_T/2$. By design, the polynomials $p_j(t)$ are matched to $f_c(t)$ and $-f_c(t)$ on the appropriate boundary points. Throughout this paper we choose $t_T = t_f/8$. An example of $q_{c,2}(t)$ and $q_{0,2}(t)$ can be seen in Figs. 2(a) and 2(b), respectively (green dashed lines).

Quasioptimal classical function $q_{c,3}(t)$. Lastly we use a quasioptimal classical auxiliary function as described in Ref. [28]. This auxiliary function is also derived via transport time-minimization in Ref. [32]. One motivation for this function is to consider the classical version of the particle transport problem. The intuitive optimal strategy in this case is to maximally accelerate the particle during the first half of the transport and maximally decelerate the particle in the second half of the transport. In Ref. [28] a sudden initial and final displacement of the potential is also included; we omit this since these displacements will occur within the smoothing intervals. We call this auxiliary function the quasioptimal classical function and define it by

$$q_{c,3}(t) = \begin{cases} 2d\left(\frac{t}{t_f}\right)^2, & 0 \leq t < \frac{t_f}{2}, \\ d\left[1 - 2\left(\frac{t}{t_f} - 1\right)^2\right], & \frac{t_f}{2} < t \leq t_f. \end{cases} \quad (29)$$

We obtain $q_{0,3}$ using Eq. (16), giving

$$q_{0,3}(t) = \begin{cases} 0, & t \leq 0, \\ 2d\left[\left(\frac{t}{t_f}\right)^2 + \frac{2}{\omega_0^2 t_f^2}\right], & 0 < t < \frac{t_f}{2}, \\ -2d\left(\frac{t}{t_f} - 1\right) - d\left(\frac{4}{\omega_0^2 t_f^2} - 1\right), & \frac{t_f}{2} < t < t_f, \\ d, & t \geq t_f. \end{cases} \quad (30)$$

We perform the same smoothing procedure as in the previous section. In the next section we investigate the impact smoothing has on fidelity for this trajectory. Examples of $q_{c,3}(t)$ and $q_{0,3}(t)$ can be seen in Figs. 2(a) and 2(b), respectively (solid red lines).

B. Derivation of eSTA control functions

To derive the eSTA control function, we must calculate $\vec{\epsilon}$ in Eq. (9). In Fig. 1(b) the improved eSTA control vector is shown schematically, with $\vec{\lambda}_s = \vec{\lambda}_0 + \vec{\epsilon}$. $\vec{\lambda}_0$ characterizes the STA control function, while $\vec{\epsilon}$ parameterizes the eSTA correction. The purpose of this distinction is to highlight how eSTA improves the control of a system, starting with an idealized STA system with the control vector $\vec{\lambda}_0$.

Now we wish to parametrize explicitly the eSTA modification and, without loss of generality, we can simplify our chosen parametrization by choosing $\vec{\lambda}_0 = \vec{0}$. This allows us to define the new improved eSTA control function $Q_j(\vec{\epsilon}, t)$ as the sum of the original STA control function and a second function $\Delta q_{0,j}(\vec{\epsilon}, t)$,

$$Q_j(\vec{\epsilon}, t) = q_{0,j}(t) + \Delta q_{0,j}(\vec{\epsilon}, t). \quad (31)$$

We now have the freedom to define $\Delta q_{0,j}$ and the $\vec{\epsilon}$ parametrization in any manner that is convenient, provided that $Q_j(\vec{\epsilon}, t)$ remains consistent with the boundary conditions of $q_{0,j}(t)$.

We define $\vec{\epsilon}$ by values that $\Delta q_{0,j}$ takes for equally spaced points in time during the transport. It is then convenient to set $\Delta q_{0,j}$ to be a polynomial,

$$\Delta q_{0,j}(\vec{\epsilon}, t) = \sum_{l=0}^{L+5} b_l t^l, \quad (32)$$

which satisfies

$$\begin{aligned} \Delta q_{0,j}(t') &= 0, & t &= 0, t_f, \\ \frac{\partial^n}{\partial t^n} \Delta q_{0,j}(t') &= 0, & t &= 0, t_f \text{ and } n = 1, 2, \\ \Delta q_{0,j}\left(\frac{l t_f}{L}\right) &= \epsilon_l, & l &= 1, \dots, L. \end{aligned} \quad (33)$$

We choose $L = 8$ in this paper as a good compromise between numerical implementation and optimization freedom; further details can be found in Ref. [12].

To implement eSTA for a given trajectory, we calculate $\vec{\epsilon}$ using Eq. (9). The states $|\chi_n(s)\rangle$ are known analytically from Eq. (19), and so the integrals G_n and K_n can be calculated for each n . We choose $N = 4$ for all the results presented in this paper as terms beyond $N = 4$ do not have an impact on the resulting fidelities or robustness, for this physical setting.

Both $\Delta q_{0,j}$ and $\vec{\epsilon}$ are illustrated in Fig. 2(c), with the STA trajectory $q_{0,1}(t)$ (dot-dashed blue line) and the improved eSTA trajectory $Q_1(\vec{\epsilon}, t)$ (solid orange line) shown for $t_f/\tau = 0.8$. The magnitude of the $\vec{\epsilon}$ components ϵ_l are shown explicitly as changes to the original STA trajectory at the times $l t_f/L$, where $l = 1, \dots, L$ and $L = 8$.

Before examining the fidelities, we note that the analytic nature of eSTA control schemes has several advantages. eSTA allows us to immediately improve analytically an existing STA control field, thus any physical intuition gained from STA can now be examined with respect to eSTA. In particular, symmetries of control functions are much more easily studied if the control functions are analytic, and eSTA can be designed to preserve the symmetries from the original STA control function. Furthermore, knowledge of symmetries that may be

required for stable control can lead to a better understanding of the physical system itself (e.g., when it is stable, are there phase transitions, etc.?). If the control function is analytic, it is also easier to see at which times the most significant corrections to the original STA control field occur. eSTA also provides several useful quantities that can be used to obtain further physical intuition behind the system dynamics; the approximation of the fidelity Eq. (5) and the gradient Eq. (7), where we highlight that evaluating these expressions does not require full time evolution.

We also underline that by using the eSTA formalism, one has the freedom to choose different starting STA protocols and can apply many different types of conditions to the eSTA analytical correction, e.g., conditions on the Fourier transform of the correction, symmetries, bounds on properties of the control field, etc. Given that calculating the eSTA control function requires little computational effort, optimization beyond eSTA can be employed easily by allowing extra parameters within the eSTA parametrization. Then a variational approach, or other numerical technique, could be used to optimize a system with a specific difficult control task.

C. Fidelities for STA and eSTA schemes

We investigate the fidelities using STA and eSTA by numerically simulating the Schrödinger equation with the lattice Hamiltonian from Eq. (11), for short transport times. We choose $m = 133$ amu (^{133}Cs), $\lambda = 866$ nm, and $\alpha = 150$, motivated by the physical values stated for lattice transport near the quantum speed limit in Ref. [28]. This choice of units corresponds to a natural time unit of $\tau = 20$ μs , where τ is approximately the quantum speed limit for this transport given in Ref. [28].

We first consider the fidelity of the STA trajectories $q_{0,1}(t)$, $q_{0,2}(t)$, and $q_{0,3}(t)$, and the results are shown in Fig. 3. The STA trajectories based on quasioptimal solutions [$q_{0,2}(t)$ and $q_{0,3}(t)$] perform better than a simple polynomial ansatz [$q_{0,1}(t)$]. We now fix a reference fidelity $F_R = 0.9$, and we see that both $q_{0,2}(t)$ and $q_{0,3}(t)$ have $F > F_R$ for $t_f/\tau \gtrsim 1.2$, while $t_f/\tau \gg 1.5$ is required for $q_{0,1}(t)$. Since the performance of STA is already optimal for $t_f/\tau \approx 1.45$, we focus on the region $t_f/\tau < 1.5$.

The fidelities for the three eSTA optimized trajectories $Q_1(t)$, $Q_2(t)$, and $Q_3(t)$ are also shown in Fig. 3. They show improvement over their corresponding STA trajectories for the transport times considered. As with the STA trajectories, the eSTA trajectories also show that the quasioptimal solutions outperform the polynomial ansatz. Furthermore, the eSTA trajectories produce higher fidelities for shorter times than the STA trajectories; $Q_{0,2}(t)$ has $F > F_R$ for $t_f/\tau \gtrsim 1.025$ and $Q_{0,3}(t)$ has $F > F_R$ for $t_f/\tau \gtrsim 0.98$.

As a side remark, we investigated whether the smoothing we performed on the trajectories had a significant impact on fidelity. As an example, in the inset of Fig. 3 the fidelities for different smoothing possibilities are shown for $Q_3(t)$. It was found that the smoothing interval t_T was not critical in obtaining high fidelities. While the highest fidelity is obtained for the fully discontinuous trajectory (dashed line), very similar results are found using a smoothing interval even as large as $t_T = t_f/8$ (dashed line). An alternative approach is to use a

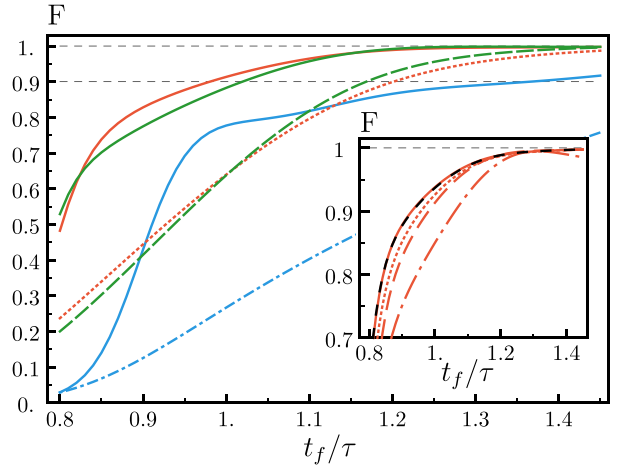


FIG. 3. Fidelity F versus final time t_f , for $\delta = 0$. The fidelities for the STA trajectories are given by the broken lines: $q_{0,1}(t)$ (dot-dashed blue), $q_{0,2}(t)$ (dashed green), and $q_{0,3}(t)$ (dotted red). The corresponding eSTA optimized fidelities are solid lines: $Q_1(t)$ (blue), $Q_2(t)$ (green), and $Q_3(t)$ (red). Inset of panel (a): Fidelity F versus final time t_f/τ using Q_3 with different smoothing options. The solid red line uses a fully discontinuous $q_{c,3}$, and the dashed black line on top of it uses $q_{c,3}$ with only the center discontinuity smoothed over a $t_T = t_f/16$ interval. The dotted red line uses $q_{c,3}$ smoothed in an interval of length $t_T = t_f/16$ around the three discontinuities and the dashed red line uses $q_{c,3}$ smoothed in an interval of length $t_T = t_f/8$ around the three discontinuities. The dot-dashed red line uses smoothing applied to $q_{0,3}$ in an interval of length $t_T = t_f/8$, starting from a fully discontinuous $q_{c,3}$.

fully discontinuous $q_{c,3}(t)$ and perform a smoothing procedure on the resulting eSTA trajectory $Q_{0,3}(t)$. However, this was found to give poorer performance, as shown in the inset of Fig. 3 (dash-dotted line). Thus, for the results in this paper the STA trajectories $q_{c,j}(t)$ were smoothed using $t_T = t_f/8$, and then the eSTA trajectories $Q_j(t)$ were calculated.

IV. eSTA CONTROL FUNCTION DEVIATION

Before starting with an examination of the robustness of eSTA, we first examine the related question of how much the eSTA control function deviates when parameters within the potential are slightly changed. We define the deviation \mathcal{C}_Q of the control function Q . The motivation for examining \mathcal{C}_Q is an expectation that if the control function does not depend strongly on a specific parameter of the potential, then this could result in stability concerning systematic errors in that parameter.

In detail, we define the deviation \mathcal{C}_Q as

$$\mathcal{C}_Q := \lim_{\delta \rightarrow 0} \frac{1}{\delta} \|Q(\delta) - Q(0)\| = \left\| \frac{\partial}{\partial \delta} Q \Big|_{\delta=0} \right\|, \quad (34)$$

where δ is some variation of the potential.

There is freedom in the choice of norm in Eq. (34), in the following we use the L_1 norm

$$\|Q(\delta)\| = \int_0^{t_f} ds |Q(\delta, s)|. \quad (35)$$

As in Eq. (31), we assume that the solution to the eSTA system with Hamiltonian $\mathcal{H}(\delta)$ takes the form

$$Q(\delta, t) = q_0(\delta, t) + \Delta q_0[\vec{\epsilon}(\delta), t], \quad (36)$$

where $q_0(\delta, t)$ is the STA control function that solves the approximate STA system, and Δq_0 is a polynomial as defined in Eq. (33). We set $\Delta q_0[\vec{0}, t] = 0$ and assume Δq_0 does not depend on the STA control function $q_0(\delta, t)$. We also have that

$$\begin{aligned} \left. \frac{\partial Q}{\partial \delta} \right|_{\delta=0} &= \left. \frac{\partial q_0}{\partial \delta} \right|_{\delta=0} + \left. \frac{\partial}{\partial \delta} \Delta q_0(\vec{\epsilon}(0), t) \right|_{\delta=0} \\ &= \left. \frac{\partial q_0}{\partial \delta} \right|_{\delta=0} + \sum_{j=1}^N \frac{\partial \Delta q_0}{\partial \epsilon_j}(\vec{\epsilon}(0), t) \left. \frac{\partial \epsilon_j}{\partial \delta} \right|_{\delta=0}. \end{aligned} \quad (37)$$

Using the definition of \mathcal{C}_Q in Eq. (34) we obtain

$$\mathcal{C}_Q := \left\| \left. \frac{\partial q_0}{\partial \delta} \right|_{\delta=0} + \sum_{j=1}^N \frac{\partial \Delta q_0}{\partial \epsilon_j}(\vec{\epsilon}(0), t) \left. \frac{\partial \epsilon_j}{\partial \delta} \right|_{\delta=0} \right\|. \quad (38)$$

By using the eSTA formalism, we can calculate $\left. \frac{\partial \epsilon_j}{\partial \delta} \right|_{\delta=0}$ explicitly as shown in Appendix A. Starting from Eq. (38), we can also derive an upper bound of the quantity \mathcal{C}_Q :

$$\begin{aligned} \mathcal{C}_Q &\leq \left\| \left. \frac{\partial q_0}{\partial \delta} \right|_{\delta=0} \right\| + \sum_{j=1}^N \left\| \frac{\partial \Delta q_0}{\partial \epsilon_j}(\vec{\epsilon}(0), t) \right\| \left\| \left. \frac{\partial \epsilon_j}{\partial \delta} \right|_{\delta=0} \right\| \\ &\leq \left\| \left. \frac{\partial q_0}{\partial \delta} \right|_{\delta=0} \right\| + \left[\max_j \left\| \frac{\partial \Delta q_0}{\partial \epsilon_j}(\vec{\epsilon}(0), t) \right\| \right] \sum_{j=1}^N \left\| \left. \frac{\partial \epsilon_j}{\partial \delta} \right|_{\delta=0} \right\|. \end{aligned} \quad (39)$$

The first term $\partial q_0/\partial \delta$ is the deviation of the STA trajectory. The second term is a measure of the eSTA dependence with respect to the control function Q , and this is the term we wish to investigate. Note that the calculation of \mathcal{C}_Q can be done fully analytically as shown in Appendix A and so requires far less computation than the numerical derivative of the fidelity which we consider in the next section. We highlight here that \mathcal{C}_Q offers potential as a tool to evaluate and classify possible eSTA trajectories in lieu of full numerical treatment. As an example, we consider a correlated error in the lattice amplitude U_0 and the wave number k_0 :

$$V_{\text{err}}^c(x, t) = U_0(1 + \delta) \sin^2 \left\{ k_0 \frac{[x - Q_j(t)]}{\sqrt{(1 + \delta)}} \right\}, \quad (40)$$

such that $\omega = \omega_0 = \sqrt{\frac{2U_0}{m}} k_0$ is kept constant. Hence the STA trajectories do not depend on δ , and we need only apply \mathcal{C}_Q to the eSTA control functions. Systematic errors in the lattice amplitude or the wave number alone are considered in following sections.

The corresponding results of \mathcal{C}_Q can be seen in Fig. 4. We find that the trajectories Q_2 and Q_3 (solid lines) show a lower deviation with changes in δ than the trajectory Q_1 . The upper bound on \mathcal{C}_Q from Eq. (39) is also shown and we see that the upper bound can be also used for classifying the different schemes. From these results, one would expect that the trajectories Q_2 and Q_3 are more stable concerning a systematic error δ . This is examined in the next section in detail and is shown to be the case.

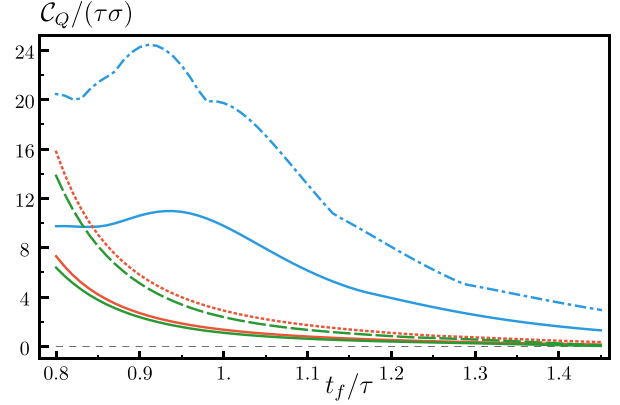


FIG. 4. Control function deviation \mathcal{C}_Q versus t_f/τ for correlated systematic error $V_{\text{err}}^c(x, t)$. Solid lines: \mathcal{C}_Q as defined in Eq. (34), using $Q_1(t)$ (solid blue), $Q_2(t)$ (solid green), and $Q_3(t)$ (solid red). Broken lines: Upper-bound definition of \mathcal{C}_Q from Eq. (39), using $Q_1(t)$ (dot-dashed blue), $Q_2(t)$ (dashed green), and $Q_3(t)$ (dotted red).

V. ROBUSTNESS TO SYSTEMATIC ERRORS

In this section we compare the robustness of the eSTA and STA trajectories by considering how the fidelity changes under three systematic errors in the lattice potential.

We first consider the correlated error V_{err}^c introduced in the last section for a specific final time and then define the sensitivity S of a given trajectory. We compare eSTA to STA using three systematic errors: the correlated error V_{err}^c , an error in the lattice amplitude V_{err}^A , and an error in the lattice wave number V_{err}^k . The amplitude and wave number errors can occur in the physical implementation of lattice potentials [33].

We define δ to be the strength of the systematic error, and the lattice amplitude error potential is given by

$$V_{\text{err}}^A(x, t) = U_0(1 + \delta) \sin^2 \{k_0[x - Q_j(t)]\}, \quad (41)$$

and the wave number error potential is

$$V_{\text{err}}^k(x, t) = U_0 \sin^2 \{k_0 \sqrt{1 + \delta} [x - Q_j(t)]\}, \quad (42)$$

with $\omega = \omega_0 \sqrt{(1 + \delta)}$ in both cases.

As a first step, we consider the correlated error V_{err}^c for a fixed final time of $t_f/\tau = 1.1$. In Fig. 5, the fidelity F versus the error strength δ is shown for the three eSTA and three STA trajectories. The STA trajectories $q_{0,2}$ and $q_{0,3}$ show similar fidelities about $\delta = 0$, and the same is true for the eSTA trajectories Q_2 and Q_3 . We see significant higher fidelities of the eSTA schemes Q_2 and Q_3 over the STA schemes $q_{0,2}$ and $q_{0,3}$, respectively. While the eSTA polynomial ansatz Q_1 has a fidelity much higher than that of the STA $q_{0,1}$, Q_1 has fidelity $F < 0.9$ for all δ in the range considered.

We see that there is no significant change in the fidelity for the eSTA trajectories in a neighborhood about $\delta = 0$, and that even for larger values of δ the eSTA trajectories maintain their higher fidelity over their related STA trajectories.

We show later that even $\partial F/\partial \delta$ at $\delta = 0$ is smaller for the eSTA trajectories Q_2 and Q_3 than for the STA trajectories $q_{0,2}$ and $q_{0,3}$ (see Fig. 6). This can also already be seen in Fig. 5, as the slopes of the eSTA lines (solid green and red line) are

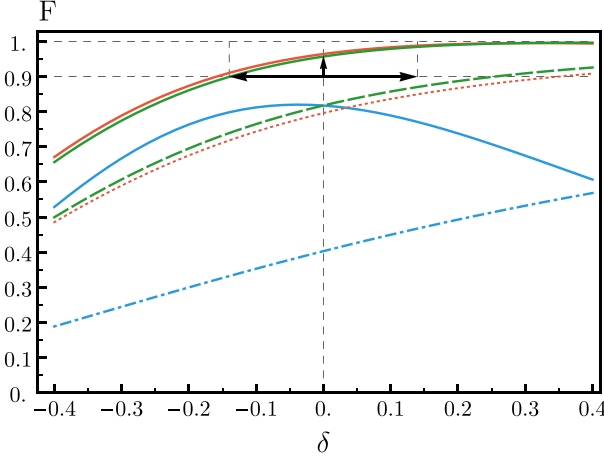


FIG. 5. Fidelity at $t_f/\tau = 1.1$ versus δ . The fidelities for the STA trajectories $q_{0,1}(t)$ (dot-dashed blue), $q_{0,2}(t)$ (dashed green), and $q_{0,3}(t)$ (dotted red). The corresponding eSTA optimized fidelities $Q_1(t)$ (solid blue), $Q_2(t)$ (solid green), and $Q_3(t)$ (solid red). The horizontal solid black arrows show $|\delta|$, such that $F(\delta) > F_R = 0.9$ using Q_2 . The vertical solid black arrow at $\delta = 0$ is $F(\delta = 0) - F_R$, again using Q_2 . These quantities are used in the definition of the systemic error bound \mathcal{B} , in Eq. (45).

less than those for the STA lines (dashed green line and dotted red line).

Note that for V_{err}^c , increasing δ corresponds with deepening of the lattice. As the lattice is deepened we find increased fidelity and stability for both Q_2 and Q_3 and $q_{0,2}$ and $q_{0,3}$.

A. Systematic error sensitivity

To examine the robustness of eSTA quantitatively for the three types of systematic errors we define the sensitivity

$$S := \left| \frac{\partial F}{\partial \delta} \Big|_{\delta=0} \right|. \quad (43)$$

A smaller value of S corresponds to a more robust protocol, i.e., less sensitivity to the error induced by δ . We evaluate S for the different errors and trajectories numerically around $\delta = 0$ by simulating the full transport. Note that, using time-dependent perturbation theory, S can be expressed as

$$S = \frac{1}{\hbar} \left| \int_0^{t_f} dt \langle \Psi_T(t) | \frac{\partial H}{\partial \delta} \Big|_{\delta=0} | \Psi_0(t) \rangle \langle \Psi_T(t_f) | \Psi_0(t_f) \rangle \right|, \quad (44)$$

where $|\Psi_0(0)\rangle$ is the initial state, $|\Psi_T(t_f)\rangle$ is the target state, and $|\Psi_0(t)\rangle$ is the time-evolved solution of the Schrödinger equation.

In the following, we evaluate both eSTA and STA for the three systematic errors stated previously. Since we are interested in trajectories that give the highest fidelity, we restrict our focus to Q_2 and Q_3 ($q_{0,2}$ and $q_{0,3}$, respectively).

In Fig. 6(c) we consider the correlated error V_{err}^c . For $t_f/\tau \geq 0.95$, eSTA shows reduced sensitivity over STA. Note that the fidelities are also higher in this t_f range (see Fig. 3). We also find that Q_2 and Q_3 in Fig. 6(c) both agree qualitatively with their analytic \mathcal{C}_Q behavior in Fig. 4.

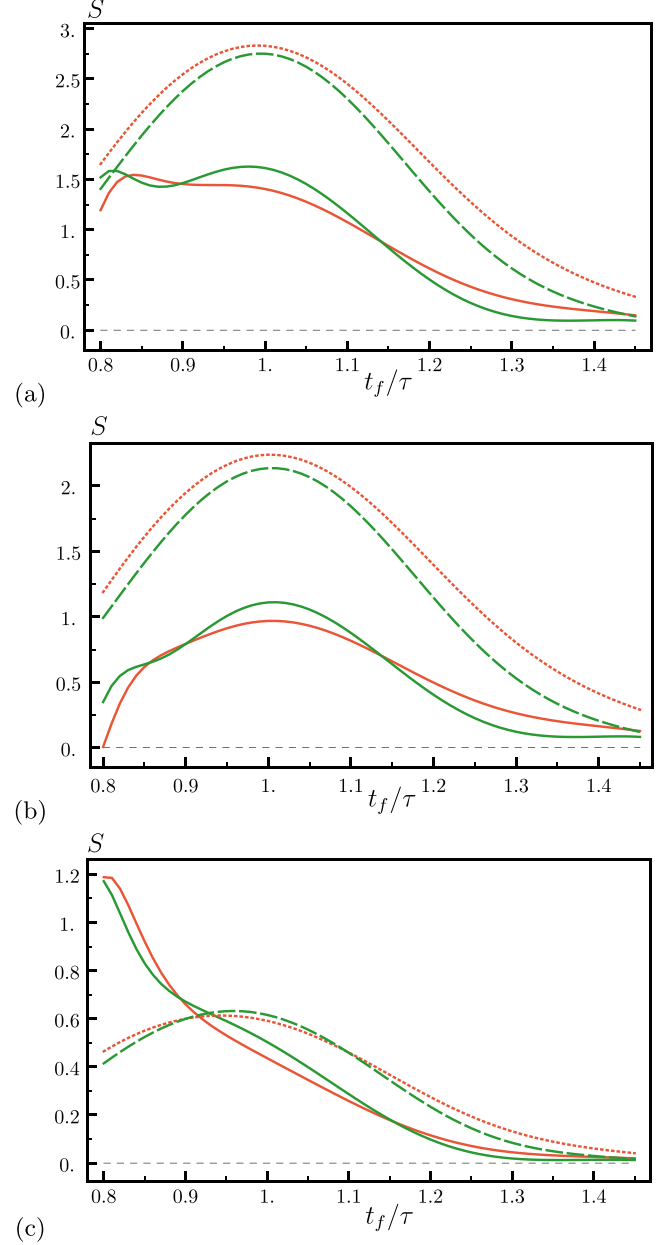


FIG. 6. Sensitivity S for systematic errors versus t_f/τ for (a) amplitude error V_{err}^A , (b) wave number error V_{err}^k , and (c) correlated error V_{err}^c . STA trajectories: $q_{0,2}$ (dashed green line) and $q_{0,3}$ (dotted red line). eSTA trajectories: Q_2 (solid green line) and Q_3 (solid red line).

We show the sensitivity of eSTA and STA versus t_f/τ for V_{err}^A in Fig. 6(a) and V_{err}^k in Fig. 6(b). For these errors, the eSTA trajectories (solid lines) generally have lower sensitivities than the STA trajectories (dashed and dotted lines).

If we first consider longer transport times, S is approaching zero for every trajectory. This behavior is expected given the adiabatic theorem; as t_f/τ approaches the adiabatic limit, small perturbations in the potential will have less impact on the instantaneous eigenstate of the system. Thus, $F \rightarrow 1$, and $S \rightarrow 0$.

For very short final times ($t_f/\tau < 1$), S becomes a less useful description of robustness since the fidelity is rapidly

decreasing for all trajectories. Hence, a more useful quantity would consider the fidelity F and sensitivity S together, and this motivates us to define a new quantity in the next section that we call the systemic error bound \mathcal{B} .

As a side remark, we note that eSTA should also provide a good initial starting point for further numerical gradient-based optimization. One would expect that the robustness of eSTA will even be improved after further numerical optimization, given the heuristic argument given in Sec. II B.

B. Systematic error bound

For practical implementation, we are interested in protocols that exceed a chosen threshold fidelity F_R while also having stability against a systematic error within a certain bound. To address these concerns, we now define a new quantity \mathcal{B} called the systematic error bound.

For a given final time, we approximate a bound \mathcal{B} on the strength of the systematic error δ , such that for $|\delta| < \mathcal{B}$ we ensure that the fidelity satisfies $F > F_R$, with F_R being a given reference fidelity. We can approximate \mathcal{B} by assuming a linear dependence of the fidelity on δ , with

$$\mathcal{B} = \begin{cases} \frac{F(\delta=0) - F_R}{S} : & F(\delta=0) > F_R, \\ 0 : & F(\delta=0) \leq F_R, \end{cases} \quad (45)$$

where for simplicity we have used the convention that $\mathcal{B} = 0$ for $F(\delta=0) \leq F_R$. The systematic error bound \mathcal{B} indicates that for a given final time the trajectory achieves fidelity above F_R for $|\delta| < \mathcal{B}$. Hence, higher values of \mathcal{B} mean higher fidelity and lower sensitivity. (In contrast, higher values of S correspond with decreased stability at a given δ .)

In Fig. 5 we show a specific example of the quantities needed to calculate \mathcal{B} . For Q_2 (solid green line), the horizontal solid black arrows in Fig. 5 show $|\delta|$ symmetric about $\delta = 0$, such that $F(\delta) > F_R = 0.9$. To calculate \mathcal{B} , we find the difference $F(\delta=0) - F_R$ (the vertical solid arrow in Fig. 5) and then scale by $1/S$. Note that, for this example, S can be seen in Fig. 6(c).

The systematic error bound \mathcal{B} is shown in Fig. 7 for the same trajectories and errors as shown previously in Fig. 6. In Fig. 7 we choose $F_R = 0.9$ and note that the quasioptimal eSTA trajectories Q_2 and Q_3 show significant improvement over the polynomial ansatz eSTA Q_1 . We include the polynomial ansatz trajectories Q_1 and $q_{0,1}$ as a reference case to highlight the usefulness of \mathcal{B} as a robustness measure. For all three errors the eSTA trajectories achieve a higher or equal \mathcal{B} over their STA counterparts, and this reflects the previous fidelity results (Fig. 3) and sensitivity results (Fig. 6).

For $t_f \rightarrow \infty$, for both the eSTA and STA error bounds $\mathcal{B} \rightarrow \infty$, since as discussed in the last section $S \rightarrow 0$ in the adiabatic limit. This is not an inherent problem with \mathcal{B} , since we are interested in applying \mathcal{B} in regions far from adiabaticity. Thus we restrict our investigation to $t_f/\tau < 1.45$, as shown in Fig. 7.

In Fig. 7 we note that the three error types produce similar \mathcal{B} behavior for each trajectory, although the magnitude of \mathcal{B} is different in each case. We find that from $t_f \geq 1$ the eSTA trajectories Q_2 and Q_3 give larger values of \mathcal{B} than the STA trajectories $q_{0,2}$ and $q_{0,3}$. These values are increasing, indicating that even when the fidelities are very high, a larger value

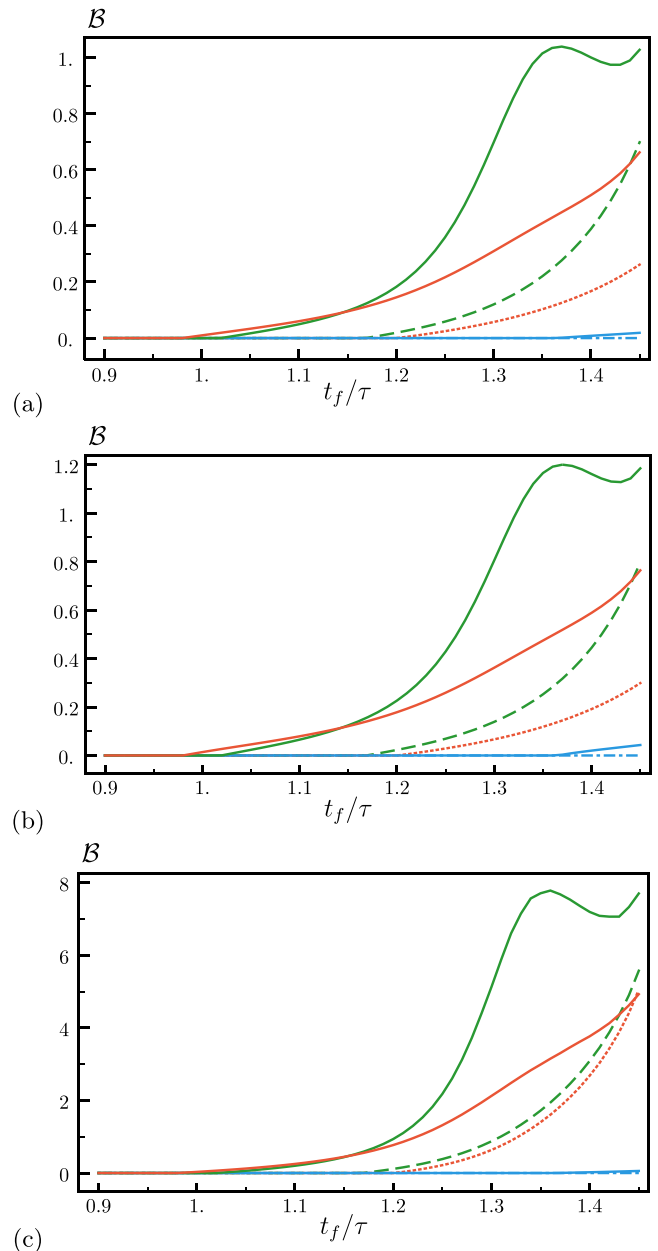


FIG. 7. Systematic error bound \mathcal{B} versus t_f/τ with $F_R = 0.9$ for (a) amplitude error V_{err}^A , (b) wave number error V_{err}^k , and (c) correlated error V_{err}^c . STA trajectories: $q_{0,2}$ (dashed green line) and $q_{0,3}$ (dotted red line). eSTA trajectories: Q_2 (solid green line) and Q_3 (solid red line).

of \mathcal{B} informs us that the eSTA sensitivity must be decreasing faster than the STA sensitivity. In this way the error bound \mathcal{B} gives us a useful comparison between trajectories, as it allows both the fidelity and the sensitivity of different trajectories to be compared simultaneously.

VI. ROBUSTNESS OF eSTA TO NOISE

We now consider the robustness and stability of eSTA with respect to noise. Specifically we consider lattice transport with classical Gaussian white noise in position and lattice

amplitude. The noise sensitivity of lattice transport using STA has previously been studied in Refs. [16,33,34].

We consider a Hamiltonian $\mathcal{H} = H_0(t) + \eta \xi(t)H_1(t)$, where η is the noise strength, $\xi(t)$ is a realization of the noise, and $H_1(t)$ is the operator coupling the system to the noise [35–37]. As shown in Appendix B a master equation can be derived [16,33]:

$$\frac{d}{dt}\rho = -\frac{i}{\hbar}[H_0, \rho] - \frac{\eta^2}{2\hbar^2}[H_1, [H_1, \rho]], \quad (46)$$

where H_0 is from Eq. (11).

We define the noise sensitivity S_N as

$$S_N = \left| \frac{\partial F}{\partial(\eta^2)} \right| = \left| \frac{1}{2} \frac{\partial^2 F}{\partial \eta^2} \right|, \quad (47)$$

and in Appendix B we use a perturbation approach to the master equation [16,38] to obtain

$$S_N = \frac{1}{\hbar^2} \left| \int_0^t ds \times \left[\text{Re} \left\{ \langle \Psi_T(s) | H_1^2(s) | \Psi_0(s) \rangle \langle \Psi_0(s) | \Psi_T(s) \rangle \right\} - |\langle \Psi_T(s) | H_1(s) | \Psi_0(s) \rangle|^2 \right] \right|, \quad (48)$$

where we use the same notation as in Eq. (44) regarding $|\Psi_0(s)\rangle$ and $|\Psi_T(s)\rangle$. We focus on transport of the ground state of the lattice, but the results in this section can be generalized naturally. The quantity S_N in Eq. (48) is useful as it allows us to measure the system's sensitivity to noise without having to numerically simulate the full open system dynamics, for example, using quantum trajectories.

Let us first consider the special case of the adiabatic limit. Let $\psi_0(x)$ be the ground state of the lattice; thus,

$$\Psi_0(t, x) = \Psi_T(t, x) = \psi_0[x - Q_j(t)]e^{i\phi(t)}. \quad (49)$$

Then Eq. (48) simplifies to

$$S_N = t_f C, \quad (50)$$

where C is given by

$$C = \frac{1}{\hbar^2} \left| \langle \psi_0 | H_1^2 | \psi_0 \rangle - |\langle \psi_0 | H_1 | \psi_0 \rangle|^2 \right|. \quad (51)$$

We again consider the error bound defined in the previous section which combines the fidelity and the sensitivity, defined as

$$\mathcal{B}_N = \begin{cases} \frac{F(\delta=0) - F_R}{S_N} & : F(\delta=0) > F_R, \\ 0 & : F(\delta=0) \leq F_R, \end{cases} \quad (52)$$

where we again adopt the convention $\mathcal{B}_N = 0$ for $F \leq F_R$. We note that in the adiabatic limit, $\mathcal{B}_N \approx \frac{1 - F_R}{C} \frac{1}{T}$, i.e., the error bound goes to zero for $T \rightarrow \infty$, where $T = t_f/\tau$ (in contrast with the systemic errors considered in the previous section).

A. Position noise

As a first example we consider position noise described by the potential

$$V_N^P = V[x - Q_j(t) - \sigma \eta \xi(t)], \quad (53)$$

with V being the lattice potential and σ the unit of space defined in Sec. III. Using only first order in η , we have

$$\begin{aligned} H_1^P &= -\sigma \frac{\partial}{\partial x} V[x - Q_j(t)] \\ &= -\sigma U_0 k_0 \sin \{2k_0[x - Q_j(t)]\}. \end{aligned} \quad (54)$$

We evaluate Eq. (48) using both STA and eSTA trajectories and plot \mathcal{B}_N in Fig. 8(a). The eSTA trajectories again outperform their STA counterparts, showing a greater \mathcal{B}_N over a larger range of shorter final times.

In Fig. 8(b) we look at larger t_f/τ and we see the STA trajectories (dashed colored lines) approach the adiabatic limit (dashed black line).

Note that when the ground state is known analytically as with the harmonic oscillator, then explicit formulas for the constant C in Eq. (51) can be found. Using the harmonic oscillator ground state as an approximation to the lattice ground state, we obtain an approximation for Eq. (51):

$$\begin{aligned} C^P &\approx \frac{1}{2} \left(\frac{U_0 k_0 \sigma}{\hbar} \right)^2 [1 - e^{-4k_0^2 \sigma^2}] \\ &= \frac{\omega_0^2 \tilde{U}_0}{4} [1 - e^{-2/\tilde{U}_0}], \end{aligned} \quad (55)$$

where $\tilde{U}_0 = U_0/(\hbar\omega_0)$. For the values considered here, $\tau^2 C^P = 0.0112$ and the approximation in Eq. (55) gives $\tau^2 C^P \approx 0.0108$.

B. Amplitude noise

For noise in the lattice amplitude we define the noise potential as

$$V_N^A = [1 + \eta \xi(t)]V[x - Q_j(t)], \quad (56)$$

with V being the lattice potential. In this case we have

$$H_1^A = V[x - Q_j(t)]. \quad (57)$$

The results for the STA and eSTA trajectories are shown Fig. 8(d). As with the position noise, the eSTA trajectories are an improvement over the STA trajectories.

Both noise sources have similar \mathcal{B}_N scales, with the position noise eSTA results showing greater improvement over STA than the amplitude noise eSTA results have over their STA counterparts.

In Fig. 8(c) the STA trajectories for amplitude noise are shown for values of t_f/τ approaching the adiabatic limit, and for $t_f/\tau > 4$ they agree.

As with the previous section, we can approximate C^A by using the analytic harmonic ground state with the lattice potential,

$$\begin{aligned} C^A &\approx \frac{1}{8} \left(\frac{U_0}{\hbar} \right)^2 e^{-4k_0^2 \sigma^2} (e^{2k_0^2 \sigma^2} - 1)^2, \\ &= \frac{\omega_0^2 \tilde{U}_0^2}{8} e^{-2/\tilde{U}_0} (e^{1/\tilde{U}_0} - 1)^2, \end{aligned} \quad (58)$$

and again $\tilde{U}_0 = U_0/(\hbar\omega_0)$. The approximation gives $\tau^2 C^A \approx 2.70 \times 10^{-3}$, while the exact value is $\tau^2 C^A = 2.97 \times 10^{-3}$.

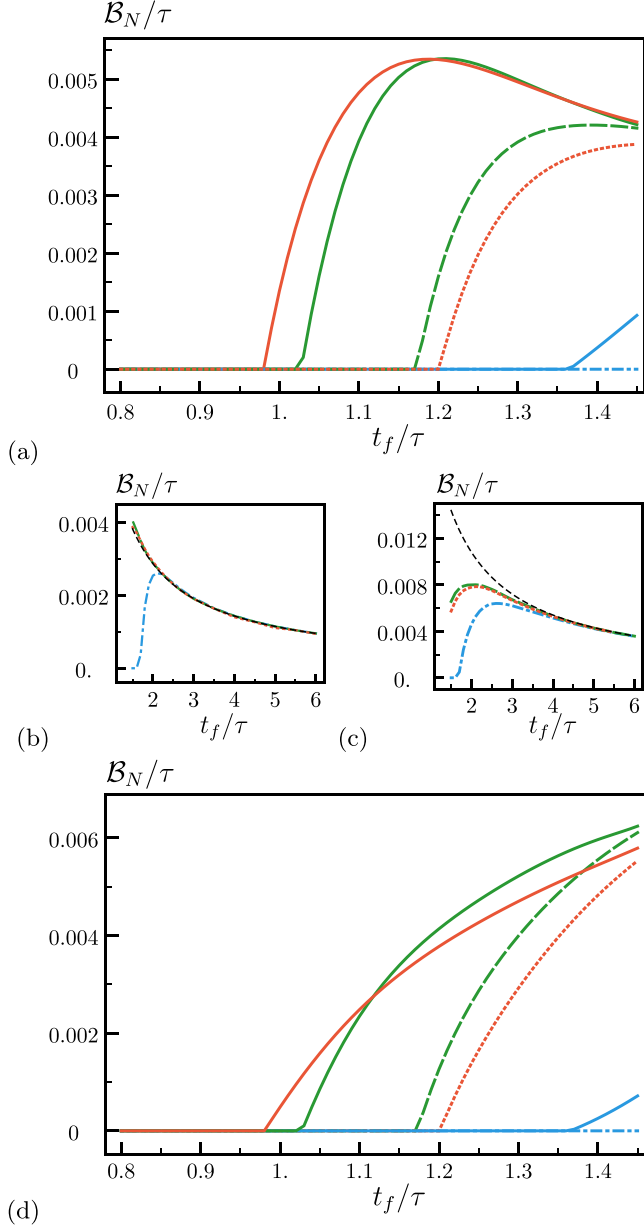


FIG. 8. Noise error bound \mathcal{B}_N versus t_f/τ with $F_R = 0.9$. (a) Position noise \mathcal{B}_N^P ; eSTA trap trajectories $Q_1(t)$ (solid blue line), $Q_2(t)$ (solid green line), and $Q_3(t)$ (solid red); STA trap trajectories $q_{0,1}(t)$ (dot-dashed blue line), $q_{0,2}(t)$ (dashed green line), and $q_{0,3}(t)$ (dotted red line). (b) Position noise \mathcal{B}_N versus larger t_f , using the STA trajectories. All the trajectories converge to the adiabatic limit (dashed black line) for large t_f . (c) Amplitude noise \mathcal{B}_N versus larger t_f , again using the STA trajectories. They also converge to the adiabatic limit (dashed black line) for large t_f . (d) Amplitude noise \mathcal{B}_N^A , with same details as in panel (a).

VII. CONCLUSION

We applied the general eSTA formalism developed in Ref. [12] to the practical problem of atom transport using an optical lattice potential, near the quantum speed limit [28]. By examining the robustness of the eSTA control schemes, we found that the eSTA transport protocols result in higher

fidelity and improved robustness against several types of systematic errors and noise errors.

We have provided a general heuristic argument that the eSTA schemes should result in higher fidelities and improved stability compared with the original STA schemes. Furthermore, we have shown strong numerical evidence of this claim by considering noise and systematic errors in the lattice potential.

Finally, we have quantified this increased robustness by defining new measures. These include an eSTA-specific evaluation tool \mathcal{C}_Q that allows possible control functions to be evaluated without full numerical treatment and a practical error bound \mathcal{B} that combines fidelity and sensitivity such that eSTA and STA control functions can be compared qualitatively. In the future the robustness of eSTA schemes and the error bound \mathcal{B} could be considered in further quantum control applications. In addition, we envisage eSTA to be a good initial starting point for numerical optimization, since further improvement in robustness is expected; this is an interesting avenue for future work.

ACKNOWLEDGMENTS

We are grateful to D. Rea for useful discussion and commenting on the manuscript. C.W. acknowledges support from the Irish Research Council (Grant No. GOIPG/2017/1846) and support from the Google Cloud Platform research credits program. A.K. acknowledges support from the Science Foundation Ireland Starting Investigator, Research Grant ‘‘SpeedDemon’’ No. 18/SIRG/5508. A.R. acknowledges support from the Science Foundation Ireland Frontiers for the Future, Research Grant ‘‘Shortcut-Enhanced Quantum Thermodynamics’’ No. 19/FFP/6951.

APPENDIX A: DERIVATION OF \mathcal{C}_Q

We can evaluate \mathcal{C}_Q using the formalism of eSTA. As before with eSTA, we write the system Hamiltonian $\mathcal{H}(\delta)$ as an expansion about the STA system that approximates it:

$$\mathcal{H}(\delta) = H_0^{\text{STA}}(\delta) + \mu \mathcal{H}_1(\delta) + \mu^2 \mathcal{H}_2(\delta) + \dots \quad (\text{A1})$$

We generalize the definitions of \vec{K}_n and G_n from the eSTA formalism to include the δ dependence in the Hamiltonian, giving

$$\vec{K}_n(\delta) = \int_0^{t_f} dt \langle \chi_n(t) | \nabla \mathcal{H}_S(\vec{\lambda}_0; t; \delta) | \chi_0(t) \rangle \quad (\text{A2})$$

and

$$G_n(\delta) = \int_0^{t_f} dt \langle \chi_n(t) | [\mathcal{H}_S(\vec{\lambda}_0; t; \delta) - \mathcal{H}^{(0)}(\vec{\lambda}_0; t)] | \chi_0(t) \rangle. \quad (\text{A3})$$

Hence we have that the eSTA control vector is given by

$$\vec{\epsilon}(\delta) \approx - \frac{[\sum_{n=1}^N |G_n(\delta)|^2] \{ \sum_{n=1}^N \text{Re}[G_n^*(\delta) \vec{K}_n(\delta)] \}}{|\sum_{n=1}^N \text{Re}[G_n^*(\delta) \vec{K}_n(\delta)]|^2}. \quad (\text{A4})$$

Now we look at the derivative with respect to δ and evaluate at $\delta = 0$:

$$\begin{aligned} \frac{\partial}{\partial \delta} \epsilon_j(0) = \epsilon_j(0) & \left(\frac{\sum_{n=1}^N 2\text{Re}[G_n^*(0) \frac{\partial}{\partial \delta} G_n(0)]}{\sum_{n=1}^N |G_n(0)|^2} + \frac{\sum_{n=1}^N \{ \text{Re}[K_{n,j}^*(0) \frac{\partial}{\partial \delta} G_n(0)] + \text{Re}[G_n^*(0) \frac{\partial}{\partial \delta} K_{n,j}(0)] \}}{\sum_{n=1}^N \text{Re}[G_n^*(0) \bar{K}_{n,j}(0)]} \right) \\ & + \frac{\sum_{j=1}^M \{ \sum_{n=1}^N \text{Re}[G_n^*(0) \bar{K}_{n,j}(0)] \sum_{n=1}^N \text{Re}[K_{n,j}^*(0) \frac{\partial}{\partial \delta} G_n(0)] + \text{Re}[G_n^*(0) \frac{\partial}{\partial \delta} K_{n,j}(0)] \}}{\sum_{j=1}^M \left| \sum_{n=1}^N \text{Re}[G_n^*(0) \bar{K}_{n,j}(0)] \right|^2}. \end{aligned} \quad (\text{A5})$$

While this expression is detailed, the individual terms are known exactly and can be calculated entirely analytically.

APPENDIX B: DERIVATION OF S_N

To consider the effect of noise on eSTA protocols, we start with a system obeying the Schrödinger equation

$$i\hbar \frac{\partial}{\partial t} |\Psi\rangle = H_0(t) |\Psi\rangle, \quad (\text{B1})$$

where $H_0(t) = p^2/2m + V(x, t)$, and V is the potential. We consider noise of the form $\eta \xi(t) H_1(t)$, where $\xi(t)$ is a given noise realization, $H_1(t)$ is the operator coupling the system to the noise, and η is the noise strength [16,35,36]. In this paper we assume that the statistical expectation $\mathcal{E}[\xi(t)] = 0$, with

$$\mathcal{E}[\xi(t)\xi(t')] = \alpha(t - t'), \quad (\text{B2})$$

where $\alpha(t - t')$ is the correlation function of the noise. Following the approach taken in Ref. [38], a master equation can be derived [16,33]:

$$\frac{d}{dt} \rho = -\frac{i}{\hbar} [H_0, \rho] - \frac{i\eta}{\hbar} [H_1, \langle \xi \rho \rangle], \quad (\text{B3})$$

where η is the perturbation parameter and ρ is the average over realizations of $\xi(t)$. Now we assume Gaussian white noise, i.e., $\alpha(t - t') = \delta(t' - t)$, and using Novikov's theorem [39], $\langle \xi \rho \rangle = -i\eta/2\hbar [H_1, \rho]$, we obtain

$$\frac{d}{dt} \rho = -\frac{i}{\hbar} [H_0, \rho] - \frac{\eta^2}{2\hbar^2} [H_1, [H_1, \rho]]. \quad (\text{B4})$$

We define

$$\begin{aligned} \frac{d}{dt} \rho_0 &= -\frac{i}{\hbar} [H_0, \rho_0], \\ |\rho_0(t)\rangle\rangle &= U_0(t, 0) |\rho_0(0)\rangle\rangle, \end{aligned} \quad (\text{B5})$$

where $|\rho_0(t)\rangle\rangle$ denotes $\rho_0(t)$ written in superoperator notation. Let

$$\mathcal{L}(t) |\rho\rangle\rangle = -\frac{1}{2\hbar^2} [H_1, [H_1, \rho]], \quad (\text{B6})$$

then [16,38]

$$\begin{aligned} |\rho(t)\rangle\rangle &= |\rho_0(t)\rangle\rangle + \eta^2 \int_0^t ds U_0(t, s) \mathcal{L}(s) U_0(s, 0) |\rho_0(0)\rangle\rangle + O(\eta^4) \\ &= |\rho_0(t)\rangle\rangle + \eta^2 \int_0^t ds U_0(t, s) \mathcal{L}(s) |\rho_0(s)\rangle\rangle + O(\eta^4). \end{aligned} \quad (\text{B7})$$

We denote the target state as $|\Psi_T\rangle$ and set $|\rho_T\rangle\rangle = |\Psi_T\rangle\langle\Psi_T|$. The fidelity is then

$$\begin{aligned} F = \langle\langle \rho_T | \rho \rangle\rangle &= \text{Tr}(\rho_T^\dagger \rho) = \langle \Psi_T | \rho(t) | \Psi_T \rangle \\ &= \langle\langle \rho_T | \rho_0 \rangle\rangle + \eta^2 \int_0^t ds \langle\langle \rho_T(s) | \mathcal{L}(s) | \rho_0(s) \rangle\rangle + O(\eta^4). \end{aligned} \quad (\text{B8})$$

We define the noise sensitivity S_N ,

$$S_N = \left| \frac{\partial F}{\partial (\eta^2)} \right| = \left| \int_0^t ds \langle\langle \rho_T(s) | \mathcal{L}(s) | \rho_0(s) \rangle\rangle \right|. \quad (\text{B9})$$

Using $\rho_0 = |\Psi_0\rangle\langle\Psi_0|$ and the explicit form of \mathcal{L} from Eq. (B6), this expression can be simplified to

$$\begin{aligned} S_N &= \frac{1}{\hbar^2} \left| \int_0^t ds \right. \\ &\quad \times \left[\text{Re} \{ \langle \Psi_T(s) | H_1^2(s) | \Psi_0(s) \rangle \langle \Psi_0(s) | \Psi_T(s) \rangle \} \right. \\ &\quad \left. - | \langle \Psi_T(s) | H_1(s) | \Psi_0(s) \rangle |^2 \right]. \end{aligned} \quad (\text{B10})$$

- [1] A. Acín, I. Bloch, H. Buhrman, T. Calarco, C. Eichler, J. Eisert, D. Esteve, N. Gisin, S. J. Glaser, F. Jelezko, S. Kuhr, M. Lewenstein, M. F. Riedel, P. O. Schmidt, R. Thew, A. Wallraff, I. Walmsley, and F. K. Wilhelm, *New J. Phys.* **20**, 080201 (2018).
[2] W. P. Schleich *et al.*, *Appl. Phys. B* **122**, 130 (2016).
[3] S. van Frank, M. Bonneau, J. Schmiedmayer, S. Hild, C. Gross, M. Cheneau, I. Bloch, T. Pichler, A. Negretti, T. Calarco, and S. Montangero, *Sci. Rep.* **6**, 34187 (2016).

- [4] A. Walther, F. Ziesel, T. Ruster, S. T. Dawkins, K. Ott, M. Hettrich, K. Singer, F. Schmidt-Kaler, and U. Poschinger, *Phys. Rev. Lett.* **109**, 080501 (2012).
[5] M. Abdelhafez, D. I. Schuster, and J. Koch, *Phys. Rev. A* **99**, 052327 (2019).
[6] J. Kelly, R. Barends, B. Campbell, Y. Chen, Z. Chen, B. Chiaro, A. Dunsworth, A. G. Fowler, I.-C. Hoi, E. Jeffrey, A. Megrant, J. Mutus, C. Neill, P. J. J. O'Malley, C. Quintana, P. Roushan, D. Sank, A. Vainsencher, J. Wenner, T. C. White *et al.*, *Phys. Rev. Lett.* **112**, 240504 (2014).

- [7] S. Machnes, E. Assémat, D. Tannor, and F. K. Wilhelm, *Phys. Rev. Lett.* **120**, 150401 (2018).
- [8] M. Murphy, L. Jiang, N. Khaneja, and T. Calarco, *Phys. Rev. A* **79**, 020301(R) (2009).
- [9] X. Chen, A. Ruschhaupt, S. Schmidt, A. del Campo, D. Guéry-Odelin, and J. G. Muga, *Phys. Rev. Lett.* **104**, 063002 (2010).
- [10] E. Torrontegui, S. Ibáñez, S. Martínez-Garaot, M. Modugno, A. del Campo, D. Guéry-Odelin, A. Ruschhaupt, X. Chen, and J. G. Muga, *Adv. At., Mol., Opt. Phys.* **62**, 117 (2013).
- [11] D. Guéry-Odelin, A. Ruschhaupt, A. Kiely, E. Torrontegui, S. Martínez-Garaot, and J. G. Muga, *Rev. Mod. Phys.* **91**, 045001 (2019).
- [12] C. Whitty, A. Kiely, and A. Ruschhaupt, *Phys. Rev. Research* **2**, 023360 (2020).
- [13] S. H. Hauck, G. Alber, and V. M. Stojanovic, *Phys. Rev. A* **104**, 053110 (2021).
- [14] A. Ruschhaupt, X. Chen, D. Alonso, and J. G. Muga, *New J. Phys.* **14**, 093040 (2012).
- [15] A. Kiely, J. P. L. McGuinness, J. G. Muga, and A. Ruschhaupt, *J. Phys. B: At., Mol., Opt. Phys.* **48**, 075503 (2015).
- [16] X.-J. Lu, J. G. Muga, X. Chen, U. G. Poschinger, F. Schmidt-Kaler, and A. Ruschhaupt, *Phys. Rev. A* **89**, 063414 (2014).
- [17] G. Ness, C. Shkedorov, Y. Florshaim, and Y. Sagi, *New J. Phys.* **20**, 095002 (2018).
- [18] L. Qi, J. Chiaverini, H. Espinós, M. Palmero, and J. G. Muga, *Europhys. Lett.* **134**, 23001 (2021).
- [19] R. Gutiérrez-Jáuregui and A. Asenjo-García, [arXiv:2104.08121](https://arxiv.org/abs/2104.08121).
- [20] A. H. Karamlou, J. Braumüller, Y. Yanay, A. Di Paolo, P. Harrington, B. Kannan, D. Kim, M. Kjaergaard, A. Melville, S. Muschinske, B. Niedzielski, A. Vepsäläinen, R. Winik, J. L. Yoder, M. Schwartz, C. Tahan, T. P. Orlando, S. Gustavsson, and W. D. Oliver, [arXiv:2107.05035](https://arxiv.org/abs/2107.05035).
- [21] I. Bloch, J. Dalibard, and W. Zwerger, *Rev. Mod. Phys.* **80**, 885 (2008).
- [22] C. Schneider, M. Enderlein, T. Huber, and T. Schaetz, *Nat. Photonics* **4**, 772 (2010).
- [23] R. B. Linnet, I. D. Leroux, M. Marcianti, A. Dantan, and M. Drewsen, *Phys. Rev. Lett.* **109**, 233005 (2012).
- [24] C. Weitenberg, S. Kuhr, K. Mølmer, and J. F. Sherson, *Phys. Rev. A* **84**, 032322 (2011).
- [25] N. B. Jørgensen, M. G. Bason, and J. F. Sherson, *Phys. Rev. A* **89**, 032306 (2014).
- [26] G. De Chiara, T. Calarco, M. Anderlini, S. Montangero, P. J. Lee, B. L. Brown, W. D. Phillips, and J. V. Porto, *Phys. Rev. A* **77**, 052333 (2008).
- [27] A. Negretti, A. Benseny, J. Mompert, and T. Calarco, *Quantum Inf. Process.* **12**, 1439 (2013).
- [28] M. R. Lam, N. Peter, T. Groh, W. Alt, C. Robens, D. Meschede, A. Negretti, S. Montangero, T. Calarco, and A. Alberti, *Phys. Rev. X* **11**, 011035 (2021).
- [29] G. Ness, M. R. Lam, W. Alt, D. Meschede, Y. Sagi, and A. Alberti, *Sci. Adv.* **7**, 52 (2021).
- [30] E. Torrontegui, S. Ibáñez, X. Chen, A. Ruschhaupt, D. Guéry-Odelin, and J. G. Muga, *Phys. Rev. A* **83**, 013415 (2011).
- [31] Q. Zhang, J. G. Muga, D. Guéry-Odelin, and X. Chen, *J. Phys. B: At., Mol. Opt. Phys.* **49**, 125503 (2016).
- [32] X. Chen, E. Torrontegui, D. Stefanatos, J.-S. Li, and J. G. Muga, *Phys. Rev. A* **84**, 043415 (2011).
- [33] X.-J. Lu, A. Ruschhaupt, and J. G. Muga, *Phys. Rev. A* **97**, 053402 (2018).
- [34] X.-J. Lu, A. Ruschhaupt, S. Martínez-Garaot, and J. G. Muga, *Entropy* **22**, 262 (2020).
- [35] E. B. Davies, *Commun. Math. Phys.* **15**, 277 (1969).
- [36] E. B. Davies, *Commun. Math. Phys.* **19**, 83 (1970).
- [37] A. Kiely, *Europhys. Lett.* **134**, 10001 (2021).
- [38] T. Yu, L. Diósi, N. Gisin, and W. T. Strunz, *Phys. Rev. A* **60**, 91 (1999).
- [39] E. A. Novikov, *J. Exp. Theor. Phys.* **20**, 1290 (1965).